



Generalised theory of polarisation modes for resonators containing birefringence and anisotropic gain

ONDREJ KITZLER,^{*} DAVID J. SPENCE, AND RICHARD P. MILDREN

MQ Photonics Research Centre, Department of Physics and Astronomy, Macquarie University in Sydney, NSW 2109, Australia

^{}ondrej.kitzler@mq.edu.au*

Abstract: Polarisation eigenmode theory is well established for laser cavities in which the principal axes for gain and polarisation elements are parallel. Here we generalise the theory to include the case for gain axes at arbitrary angle to the birefringence, which is the case for Raman lasers based on cubic-class gain crystals that contain stress-induced birefringence. The theory describes regimes dominated by gain, linear or circular birefringence, and the intermediate regime in which elliptically polarised output modes are obtained. Previously reported behaviour for diamond Raman lasers are found to be in accord with the findings. Design criteria are obtained to enable prediction of polarisation behaviour as functions of birefringence and resonator design.

© 2019 Optical Society of America under the terms of the [OSA Open Access Publishing Agreement](#)

1. Introduction

The mode properties of lasers are determined by the resonator boundary conditions and the effects of intracavity elements on amplitude and phase. In the case of polarisation modes, the analysis is simplified when the axes of birefringent elements are parallel to those of the gain. One notable exception is laser media suffering radial thermally-induced stress birefringence to produce complex output beam patterns including the characteristic Maltese cross pattern of ref [1]. Though this specific case has been solved [1, 2], there is another class of problems involving linearly anisotropic gain and birefringence but with non-collinear axes. Such a scenario has been recently identified in diamond Raman lasers (DRLs) in which the crystal contains in-grown stress birefringence [3].

Calculation of polarisation modes of such anisotropic resonators are often found using mode theory (see e.g., [4]) combined with a Jones matrix formalism (see e.g., [5]). Eigenvector solutions of the resonator round-trip matrix represent the polarisation states and the corresponding eigenvalues enable determination of the polarisation mode that experiences the highest net gain and thus establishes first in the cavity. Although some laser gain crystals, such as Nd:YVO₄, show anisotropy in their emission cross-section, the eigensolution analysis is determined by the passive elements [6], since they are either the dominating effect or the gain axes are parallel with the axes of the dominant polarising element. In systems with strong polarisation mode competition, such as intra-cavity frequency doubled solid-state lasers, an effective emission cross section, and thus threshold, can be defined for each eigensolution [7]. Effects of gain anisotropy in presence of birefringence have been studied numerically for microchip lasers [8] and VCSELs [9]. Coupled laser-level rate equations for two orthogonal cavity eigensolutions explain the polarisation dynamics of these lasers. In the case of spin injected VCSELs, their gain exhibits small circular anisotropy which has been recently shown to reveal complex dynamics in the polarisation modes [10–12].

A specific example of systems with strong gain anisotropy is crystalline Raman lasers [13]. Most of the practical Raman crystals are naturally birefringent [14], however, even isotropic Raman crystals such as diamond, silicon, and Ba(NO₃)₂, which are cubic [14], contain stress induced

birefringence or the resonator consists of other anisotropic elements or components with stress induced birefringence of an arbitrary direction. An analytical model for the polarisation behaviour has not yet been presented for lasers possessing linearly anisotropic gain and non-collinear birefringence axes.

In this paper we extend the Jones formalism to include linearly anisotropic gain and derive the Jones matrix for the specific case of diamond. The theory is applied to standing wave and ring resonators containing stress induced linear and circular birefringence in the crystal. We show that the fully analytical calculations explain the observed difference in polarisation behaviour of pulsed and continuous wave (cw) DRLs.

2. General theory

Jones matrices describe how individual optical elements in the laser resonator act upon the polarisation state of the circulating beam. Jones matrices for standard optical elements can be found e.g., in [15]. The Jones matrix for a birefringent material with fast axis parallel to a local x axis is defined as

$$B = \begin{pmatrix} e^{-i\frac{\xi}{2}} & 0 \\ 0 & e^{i\frac{\xi}{2}} \end{pmatrix}, \quad (1)$$

where $\xi = 2\pi L(n_y - n_x)/\lambda$ is the phase difference induced by a birefringent plate of length L with refractive indices n_x and n_y in x and y axis.

For a gain medium for which two orthogonal polarisation components of generated laser field amplify independently, we define the Jones matrix of gain as

$$G = \begin{pmatrix} e^{G_0\gamma_1} & 0 \\ 0 & e^{G_0\gamma_2} \end{pmatrix}, \quad (2)$$

where G_0 is the conventional single pass gain with separated normalised amplification weightings $\gamma_{1,2}$.

In a laser resonator above threshold, G_0 is fixed by a lasing threshold condition. Assuming $\gamma_1 \geq \gamma_2$, that condition is

$$Re^{2G_0\gamma_1} = 1 \quad (3)$$

$$G_0 = \frac{1}{\gamma_1} \ln \left(R^{-\frac{1}{2}} \right), \quad (4)$$

where the effective cavity reflectivity R accounts for transmission of all mirrors as well as other parasitic losses. Using Eq. (4) the gain matrix in a symmetrical form is

$$G = \begin{pmatrix} e^{\frac{\Gamma}{2}} & 0 \\ 0 & e^{-\frac{\Gamma}{2}} \end{pmatrix}, \quad (5)$$

where $\Gamma = 1/\gamma_1 \ln(R^{-\frac{1}{2}}) \cdot (\gamma_1 - \gamma_2)$. In this form the average amplification factor $e^{1/\gamma_1 \ln(R^{-\frac{1}{2}}) \cdot (\gamma_1 + \gamma_2)/2}$ was removed.

A gain material containing only a pure linear birefringence can be modelled as a separate gain and an arbitrarily oriented waveplate as the birefringence and gain matrices commute. The roundtrip matrix of a resonator containing gain and linear birefringence is

$$M = GR(\tau)BR(-\tau)R(\tau)BR(-\tau)G, \quad (6)$$

where $R(\tau)$ is a counter-clockwise rotation matrix which accounts for the angle τ between the fast axis of the birefringence and the gain basis. Eigensolutions of the matrix M are two orthogonal eigenvectors v_1 and v_2 and eigenvalue κ_1, κ_2 . The polarisation of the established laser mode is given by the largest eigenvector.

3. The anisotropic Raman gain in crystals of F_{2g} symmetry

We now derive the amplification factors $\gamma_{1,2}$ for crystals of cubic symmetry (specifically diamond), which has a triply degenerated Raman mode and features strongly anisotropic gain [13]. The gain maximizes for coincident pump and Stokes polarisations aligned to a $\langle 111 \rangle$ direction [16]. Note that the $\langle 111 \rangle$ directions are not orthogonal (70.6°) as shown in Fig. 1. In arbitrary bases

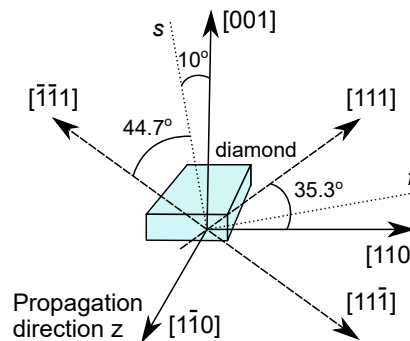


Fig. 1. Crystallographic directions in diamond with respect to usual propagation direction used in Raman lasers and an example of birefringence fast f and slow s axis orientation.

the power flow from pump to Stokes fields describe four coupled equations [17]

$$\begin{aligned}\frac{dS_k}{dz} &= \frac{g}{2} \sum_{ijl} \chi_{ijkl}^{(3)} S_i P_j P_l^* \\ \frac{dP_l}{dz} &= -\frac{g}{2\eta} \sum_{ijk} \chi_{ijkl}^{(3)} S_i P_j S_k^*,\end{aligned}\quad (7)$$

where S and P are amplitudes of the Stokes and pump field, respectively, g is the small signal Raman gain coefficient, $\eta = \lambda_p/\lambda_s$ is the quantum defect of the inelastic Raman scattering, where λ_s and λ_p are the Stokes and pump wavelengths, $\chi_{ijkl}^{(3)}$ are normalised components of the third order Raman susceptibility tensor accounting only for coupling differences between the fields and indexes i, j, k, l represent all permutations of local x and y axes.

We limit the discussion to cases near lasing threshold, in which the effects caused by uneven depletion of P_1 and P_2 and resulting pump polarisation rotation can be neglected. If the pump basis orientation is aligned with the input linear polarisation direction, the P_2 is zero and Eqs (7) simplify to

$$\begin{aligned}\frac{dS_1}{dz} &= \frac{g}{2} \left(\chi_{11'11}^{(3)} S_1 P_{1'} P_{1'}^* + \chi_{21'11}^{(3)} S_2 P_{1'} P_{1'}^* \right) \\ \frac{dS_2}{dz} &= \frac{g}{2} \left(\chi_{21'21}^{(3)} S_2 P_{1'} P_{1'}^* + \chi_{11'21}^{(3)} S_1 P_{1'} P_{1'}^* \right) \\ \frac{dP_{1'}}{dz} &= -\frac{g}{2\eta} \sum_{i,k=1,2} \chi_{i1'k1}^{(3)} S_i P_{1'} S_k^*.\end{aligned}\quad (8)$$

As the polarisation bases for the pump and the Stokes fields are not required to coincide, primes were added to the pump basis labels in Eqs. (8) to discern it from the Stokes basis. As shown below, it is useful to choose a different Stokes basis. We calculate the $\chi^{(3)}$ terms as a function of the pump and Stokes basis angles α and β , respectively, using the tensor for diamond [13]. The ‘direct’ susceptibility components $\chi_{11'11'}^{(3)}$ and $\chi_{21'21'}^{(3)}$, where the pump interacts with S_1 and S_2 independently, are [17]

$$\chi(\alpha, \beta) = \sum_{i=1,2,3} (e_s(\beta) R_i e_p(\alpha)) (e_s(\beta) R_i e_p(\alpha))^* \quad (9)$$

where the angles α and β are with respect to the $[110]$ direction and e_s and e_p are unit vectors pointing in the directions of Stokes and pump polarisations, respectively. The ‘cross coupling’ terms $\chi_{21'11'}^{(3)}$ and $\chi_{11'21'}^{(3)}$, where the amplification of S_1 and S_2 depend on each other, are

$$\chi_{\text{cross}}(\alpha, \beta) = \sum_{i=1,2,3} (e_s(\beta) R_i e_p(\alpha)) (e_s(\beta + \pi/2) R_i e_p(\alpha))^*, \quad (10)$$

Equations (8) simplify when choosing a basis for which the χ_{cross} terms are zero (so that the Stokes field components are independently amplified). Figure 2 shows the calculation of χ and χ_{cross} for all combinations of pump and Stokes bases orientations α and β . It is seen that, for every pump polarisation, there exists a Stokes basis in which the cross terms vanish (see Fig. 2(b)) and are 90° apart. For example, for a pump polarisation angle of $\alpha = 90^\circ$, the χ_{cross} terms are

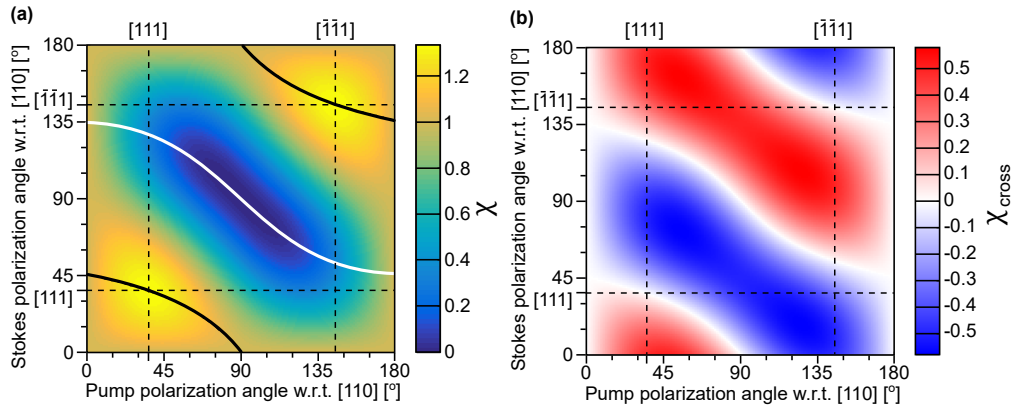


Fig. 2. (a) χ as a function of pump and Stokes polarisation angles. Full black and white lines show maxima γ_1 and minima γ_2 , respectively. (b) χ_{cross} as a function of pump and Stokes polarisation angles.

zero for the Stokes basis angle $\beta = 0^\circ$. For this choice, the polarisations amplify independently with gains proportional to maxima and minima values of χ (shown as black and white full lines in Fig. 2(a)). With such directions chosen as a Stokes basis Eqs. (8) reduce to

$$\begin{aligned} \frac{dS_1}{dz} &= \frac{g\gamma_1}{2} S_1 P_1 P_1^*, \\ \frac{dS_2}{dz} &= \frac{g\gamma_2}{2} S_2 P_1 P_1^*, \\ \frac{dP_1}{dz} &= -\frac{g}{2\eta} (\gamma_1 S_1 P_1 S_1^* + \gamma_2 S_2 P_1 S_2^*). \end{aligned} \quad (11)$$

The maxima γ_1 and minima γ_2 of χ are found by parametrizing Eq. (9) and finding its extremes. The solutions for γ_1 and γ_2 are

$$\begin{aligned}\gamma_1 &= \cos^2 \left\{ \frac{1}{2} \arctan [2 \cot(\alpha)] \right\} \cos^2(\alpha) + \sin^2 \left\{ \alpha + \frac{1}{2} \arctan [2 \cot(\alpha)] \right\} \\ \gamma_2 &= \cos^2 \left\{ \frac{\pi}{2} + \frac{1}{2} \arctan [2 \cot(\alpha)] \right\} \cos^2(\alpha) + \sin^2 \left\{ \frac{\pi}{2} + \alpha + \frac{1}{2} \arctan [2 \cot(\alpha)] \right\}, \quad (12)\end{aligned}$$

Eqs. (12) describe the black and white lines in Fig. 2(a). Since the coupling coefficients are normalised to the value of pump polarisations parallel to [110] direction, γ_1 grows from 1 to 4/3 and falls back to 1, and γ_2 decreases from 1 through 1/3 to 0 as the pump polarisation is rotated from 0° through 35.3° to 90°, respectively. With these simplifications, the gain matrix G takes the form of Eq. (2) allowing the solution procedure of Sec. 2. G is a function of only the combined loss and reflectivity of the mirrors R and the angle of the pump polarisation α , which in turn defines the Stokes basis and amplification coefficients $\gamma_{1,2}$.

4. Model results

The eigenvectors and eigenvalues of the roundtrip matrix M (Eq. (6)) predict the output Stokes polarisation dependencies. M is a function of the four parameters; the birefringence phase difference ξ , the angle between the birefringence fast axis and Stokes bases τ , the angle of the pump polarisation α which defines the coupling parameters γ_1 and γ_2 , and the effective reflectivity of the mirrors R that determines steady-state gain strength.

The impact of ξ is the strongest when the Stokes bases is 45° to birefringence axes and is zero if they coincide. The effect of Γ increases from zero to $\ln(R^{-1/2})$ as the pump polarisation direction changes from 0° to 90°. The relative strength of Γ and ξ distinguishes several cases. When the gain term dominates, (i.e., $\Gamma \gg \xi$), the cavity eigenvectors are linear polarisations aligned with the Stokes basis. When birefringence dominates ($\Gamma \ll \xi$), the eigenvectors are linear polarisations in the directions of the birefringence fast and slow axis and for $\Gamma \approx \xi$ the output polarisations are elliptical. The following sections discuss model results for the three cases and a case involving the addition of circular birefringence.

Note that for $\Gamma = 0$, the solutions are eigenvectors along the birefringence axes directions with identical eigenvalue and the laser can operate on either of them. If ξ is also zero, the solution of the roundtrip matrix is the identity for which all eigenvectors are solutions with identical eigenvalue. Experiments have shown that linear polarisations are produced under such conditions, but with direction that changed randomly from pulse to pulse [16].

4.1. Output polarisation determined by gain: Case $\Gamma \gg \xi$

In this case the solutions are linear polarisations along the Stokes basis where output Stokes is linearly polarised along the direction β of the highest normalised gain component γ_1 , with $\beta = 1/2 \arctan(2 \cot(\alpha))$. Figures 3(a)-(d) indicate the polarisation, ellipticity and angle for all pump polarisation angles and for birefringence phase shift increasing up to 100 mrad. The gain dominated behaviour is shown in the bottom row in Figs. 3(a)-(d) (the 0° pump case was excluded). For pump polarisation rotated from 0° to 90° the output polarisation rotates in opposite direction from 45° to 0°. The pump and output polarisations coincide for <111> directions, at 35.3° and 144.7°. Such behaviour is typical for pulsed DRLs using relatively low R [16]. Note that output polarisations beyond 45° are not obtained for any pump polarisation.

4.2. Output polarisation determined by linear birefringence: Case $\Gamma \ll \xi$

Under this condition the cavity eigenvectors are linear polarisations aligned with the birefringence fast and slow axes as shown in top rows of Fig. 3(a)-(d). The gains associated with each axis

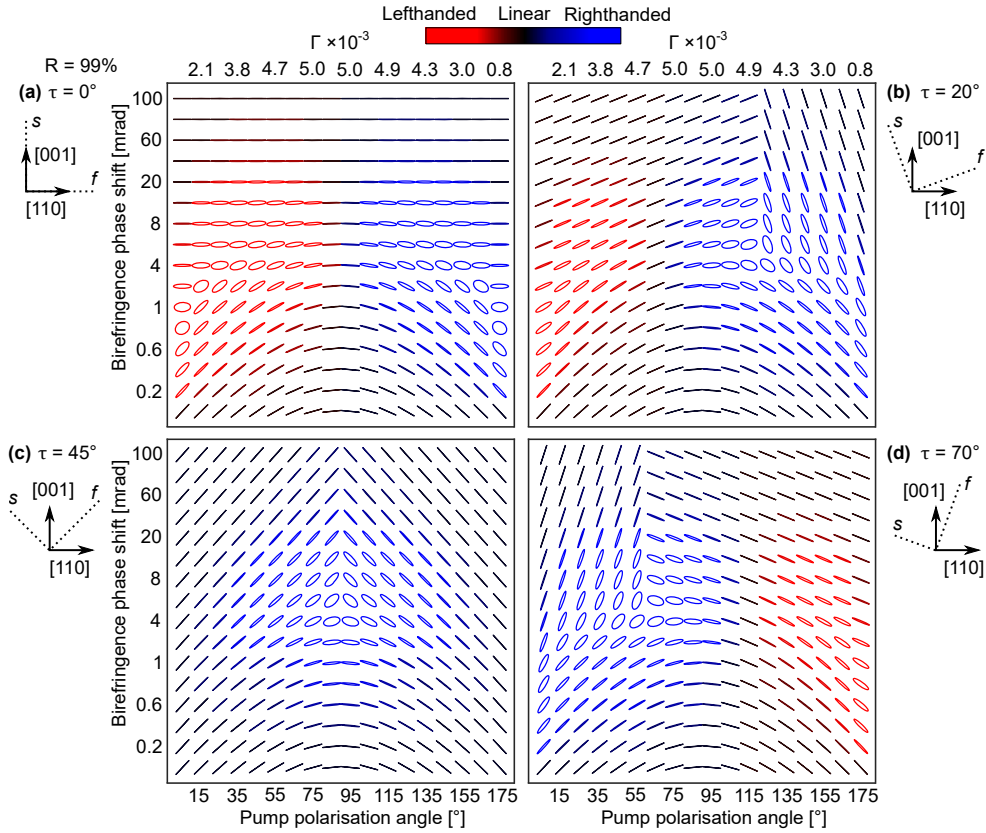


Fig. 3. Output polarisations shown as ellipses as a function of linear pump polarisations angles and birefringence phase shift. Top axis indicates corresponding Γ . The colours red/blue indicate left/right handedness. $R = 99\%$ and $\tau = 0^\circ, 20^\circ, 45^\circ$, and 70° in (a), (b), (c), and (d), respectively.

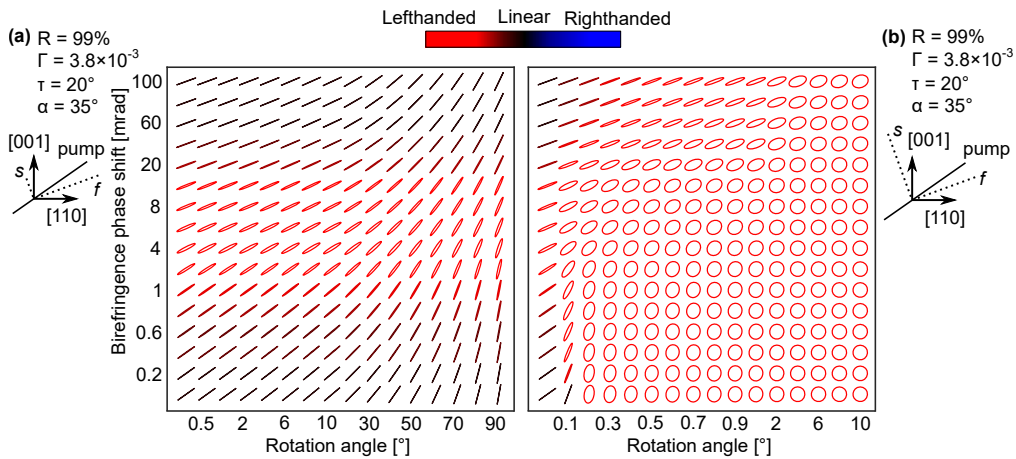


Fig. 4. Output polarisations shown as ellipses as a function of induced rotation angles and birefringence phase shift. (a) and (b) show the polarisation behaviour for $R = 99\%$, $\Gamma = 3.8 \times 10^{-3}$, $\tau = 20^\circ$, and $\alpha = 35^\circ$ for a linear and ring cavity, respectively.

direction, and therefore which polarisation lases, is dependent on the pump polarisation and fast axis direction. In Fig. 3(a) the output polarisation is always horizontal, in 3(b) and 3(d) the polarisations flip at 120° and 60° , respectively and in 3(c) the flip occurs at 90° . There is also a flip when the pump polarisations cross $0^\circ/180^\circ$. The switching between polarisations is well produced in experiments as shown in Sec. 4.5. Vertical output polarisations are not obtained even for a vertical fast axis, as in the high gain case; however, all other orientations are possible.

The pump polarisation at which the output polarisation flips occurs at the crossing points where the gain for one axis surpasses the other. Figure 5(a) shows the normalised gain as a function of pump polarisation angle and birefringence fast axis direction. The region where the gain is highest for the slow axis direction is highlighted by white stripes. For any pump polarisation, maximum gain (indicated by dashed black lines) is achieved when birefringence axes coincide with the Stokes bases.

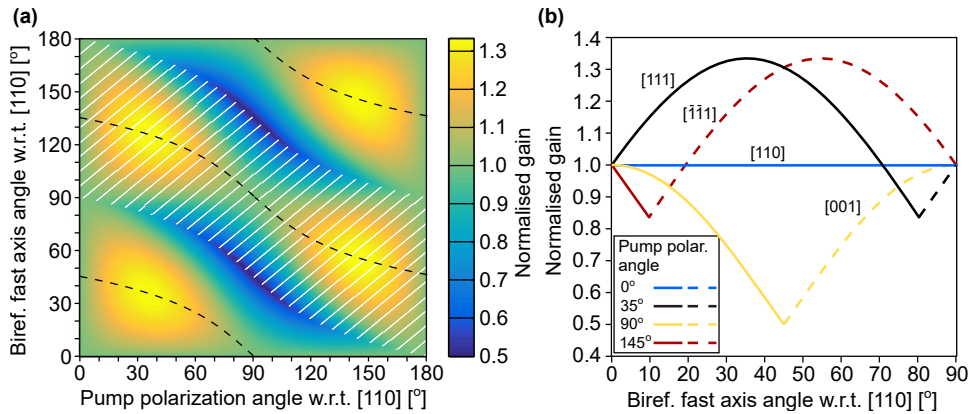


Fig. 5. (a) Normalised gain as a function of pump and birefringence fast axis angle τ for strong birefringence $\xi = 15$ mrad and low gain $R = 99\%$. Black dashed lines indicate gain maxima. White stripes indicate the region where the output polarisation is parallel to the slow birefringence axis. (b) Gain as a function of birefringence fast axis angle for pumping polarisations parallel to the $[110]$, $[111]$, $[001]$, and $[\bar{1}\bar{1}0]$. The lines change from full to dashed for the Stokes polarisation parallel to fast and slow axis, respectively.

Figure 5(b) shows vertical cuts through Fig. 5(a) for pump polarisations aligned to crystal directions of high symmetry. For any birefringence orientation (except 0° and 90°) the highest gain is obtained for the pump polarisation parallel to the $\langle 111 \rangle$ axis that is closest to a fast or slow birefringence axis. The maximum difference in gain, and thus threshold, between the two $\langle 111 \rangle$ directions is 26% for birefringence fast axis oriented at 10° and 80° . At 10° , for example (as in Fig. 1), the birefringence axes are 45° from $[\bar{1}\bar{1}1]$ and 25° from $[111]$ direction and therefore for $[\bar{1}\bar{1}1]$ pumping the Stokes polarisation direction is pulled the furthest from its original direction unperturbed by birefringence.

4.3. Output polarisation determined by balance between linear birefringence and gain: Case $\Gamma \approx \xi$

For approximately balanced gain and birefringence, the output is elliptical as shown in Figs. 3(a)-(d) as red (left-handed) and blue (right-handed) ellipses. For intermediate values of ξ , the ellipticity strongly depends on pump polarisation due to the resultant effect on Γ and the angle between the birefringence and Stokes bases. The output becomes linear when the Stokes high gain axis coincides with one of the birefringence axes. In that case the output polarisation remains unchanged for any phase shift value as it does not interact with the birefringence. Thus elliptical

states are observed in the transition region where $\Gamma \approx \xi$ and when the maximum gain direction is away from the birefringent axes.

As a specific example we consider the situation for a birefringence fast axis at $\tau = 20^\circ$ (Fig. 3(b)). For pump polarisation close to 0° , the Stokes is elliptical for ξ between 0.2 mrad and 4 mrad. As the pump angle is increased, Γ also increases and, correspondingly, elliptical outputs are obtained only for larger values of ξ . For fixed ξ , the major effect of increasing the pump polarisation angle is to shift the Stokes basis towards τ . The polarisation is purely linear for the pump angle of 65° , for which the Stokes basis coincides with τ . Further increasing the pump angle ultimately leads again to elliptical output but with opposite handedness and a flip of the major axis from fast to slow birefringence axis at a pump angle of 120° .

The transition from low to high birefringence is shown in more detail by plotting ellipticity as a function of R and the birefringence phase shift. Figure 6 shows ellipticity for two cases: Fig. 6(a) for pump polarisation close (within 5°) to the $[110]$ direction for which $\gamma_1 \approx \gamma_2 \approx 1$ and Fig. 6(b) for pump polarisation aligned with $[001]$ where $\gamma_1 = 1$ and $\gamma_2 = 0$. For both plots, the birefringence fast axis is at 45° with respect to high gain axis γ_1 (i.e., 0° and 45° , respectively) to induce the highest ellipticity. Note, however, that the maximum ellipticity never reaches 1. Below the region of high ellipticity (gain dominated regime) the output polarisation tends to linear along the Stokes basis high gain axis. Conversely, above the region (birefringence dominated regime), the polarisation tends to the birefringence axis with higher gain.

The Γ value as a function of R is plotted on Figs. 6(a)-(b) (dashed line), confirming that $\Gamma \approx \xi$ is the condition needed to produce strongly elliptical output. Γ deviates from this condition for small values of R and large gain difference. For increasing R (decreasing Γ) the phase shift required to induce ellipticity and ultimately flip the polarisation from the high gain to the birefringence axis is smaller. The slope of the peak ellipticity line is smaller in Fig. 6(a) than 6(b) due to the smaller gain difference and thus the birefringence dominates for smaller ξ .

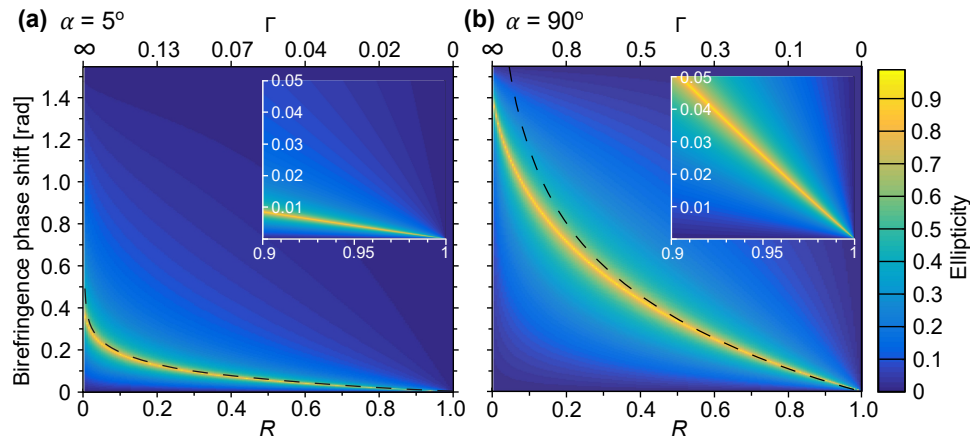


Fig. 6. Ellipticity of the Stokes mode as a function of R and birefringence phase shift ξ for pump polarisation angles of (a) 5° and (b) 90° . The dashed black line indicates the magnitude of the gain difference Γ (also shown as the top axis) as a function of R on the ξ axis. The insets show magnified regions for typical values observed in diamond and used in cw DRLs.

The insets of Fig. 6(a) and 6(b) show the ellipticity for typical values used in cw DRLs. The reflectivities range from 99.5% to about 90% depending on pump power [18, 19] and birefringences at $1 \mu\text{m}$ wavelength are about 0.05 rad (but can be as high as 0.5 rad) for materials typically used in lasers [3]. These results indicate that elliptical output is predicted for experimental parameters of $R = 99\%$ and $\xi = 5$ mrad, for example, when using a pump

polarisation of 90°.

4.4. Optical rotation

Some CVD-grown single crystal diamonds show evidence of optical rotation as a result of the compound effect of crystal stress induced birefringence with varying orientation in the propagation direction [3]. Such an element, represented as a sequence of randomly oriented wave-plates, is equivalent to a single wave-plate and a rotator [20]. However, since the rotator matrix is non-commutative with the gain and birefringence matrices, a single matrix describing all effects is required to enable calculation of the cavity eigenmodes. Such a matrix can be obtained, following the derivation in [21], by dividing the medium into thin layers of separate birefringence, gain and optical rotation effects. Since the change induced in each layer is small, the exponential functions in gain and birefringence matrices and trigonometric functions in the rotation matrix can be replaced by low order Taylor expansions. Such matrices commute and, in the limit of zero thickness, combine into the overarching matrix J as

$$J = \begin{pmatrix} \cos \frac{T}{2} - \frac{i\xi \cos(2\tau) - \Gamma}{T} \sin \frac{T}{2} & \frac{\Theta - i\xi \sin(2\tau)}{T} \sin \frac{T}{2} \\ -\frac{\Theta + i\xi \sin(2\tau)}{T} \sin \frac{T}{2} & \cos \frac{T}{2} + \frac{i\xi \cos(2\tau) - \Gamma}{T} \sin \frac{T}{2} \end{pmatrix}, \quad (13)$$

where $\Theta/2 = \theta$ is the circular birefringence with induced optical rotation θ , $T = \sqrt{\xi^2 + \Theta^2 + \Gamma^2}$ and dichroism terms were neglected for simplicity. Setting $\Theta = 0$ in J retrieves the result from Eq. (6) for small birefringence and gain as required.

In a standing wave resonator, the rotation angle in matrix J changes sign on the second pass. However, because the gain, linear birefringence, and optical rotation act upon the field simultaneously, the rotation is not completely cancelled per round trip. The outcome is that any Stokes polarisation is rotated exactly by half of the optical rotation angle, as shown in Fig. 4(a) for the example parameters of 35° and 20° for the pump and the birefringence fast axis angles, respectively.

In contrast, in a ring resonator, the rotation accumulates for each round-trip and thus even a small amount of rotation results in an elliptical output polarisation. Referring to Fig. 4(b), for $\Gamma \gg \xi$ (bottom rows), the polarisation is highly elliptical even for small optical rotation angles and with its major axis rotating towards 90°. For $\Gamma \ll \xi$ (top rows), the ellipticity is induced only for much larger rotation values and the major axis remains oriented along the birefringence axis. These results indicate that the ellipticity of output for ring resonators will be highly susceptible to circular birefringence. For such conditions the normalised gain changes from 1 to 0.5 as the pump polarisation angle changes from horizontal to vertical. The output polarisation handedness depends on the direction of optical rotation and also the strength and orientation of the linear birefringence. The normalised gain of the rotated polarisations in a linear resonator follows identical rules to Fig. 5(a).

4.5. Experimental comparison ($\Gamma \gg \xi$, $\Gamma \ll \xi$)

We verify the validity of the model against the polarisation measurements of a DRL similar to that reported in [16] but operated close to threshold (case $\Gamma \gg \xi$) and the DRL in [3] (case $\Gamma \ll \xi$). Measured and modelled polarisation angles are shown in Fig. 7 for (i) $\Gamma \gg \xi$ and for $\Gamma \ll \xi$ for three birefringence axis directions ((ii), (iii), and (iv)). The modelled polarisations closely match the measurements, except for one point in (iii), where the experiment switches direction later than predicted, most likely due to inaccurate determination of the birefringence axis direction or magnitude of optical rotation.

The role of birefringence magnitude and direction is analysed in more detail by plotting the observed output polarisations on the gain map of Fig. 5 as displayed in Fig. 8. For (i) the Stokes

output is polarised along the high-gain directions as expected. The measurements closely follow the maximum of the gain γ_1 even for pump angles approaching 0° where a transition to unstable or random polarisation directions is expected. The absence of such behaviour may have been caused by a coincidence of the particular orientation of the birefringence axis close to 45° .

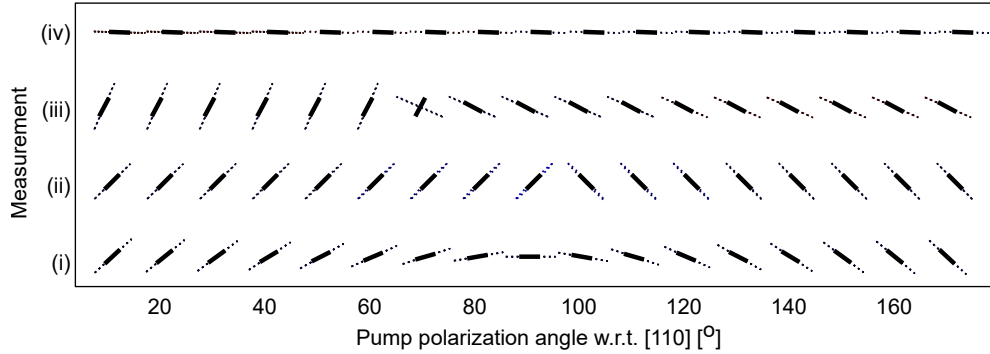


Fig. 7. Measured Stokes polarisation angles (full thick lines) compared to modelled Stokes polarisations (dashed). (i) this work, $R = 0.3$, $\xi = 0.3$ rad, τ unknown; (ii), (iii), (iv) from [3], $R = 0.99$ (R used was 99.5% plus 0.5% additional roundtrip loss), $\xi = 0.06$ rad, 0.2 rad, 0.27 rad, $\tau = 45^\circ$, 71° , 1.7° , and $\theta = 1.25^\circ$, 9.15° , 6.6° , respectively, measured by Mueller polarimetry.

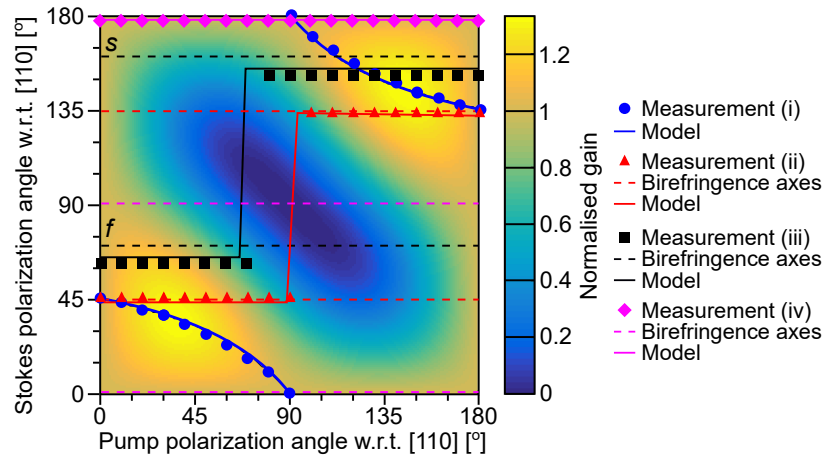


Fig. 8. Stokes output polarisation angle as a function of pump polarisation angle. Dashed lines show fast f and slow s axis of the linear birefringence determined by Mueller polarimetry. Blue circles and full line show measured and modelled Stokes polarisation angles for given pump polarisation angles for $\Gamma \gg \xi$. The triangle, square and diamond symbols show measurements (ii), (iii), (iv) corresponding to spots A, C, D in [3] respectively and show the opposite case of $\Gamma \ll \xi$ for varying values of birefringence and its orientation. Full lines of the same colour are corresponding modelled results and dashed lines indicate the orientation of the linear birefringence.

In the birefringence dominated regime the model correctly predicts the starkly contrasting behaviour in which the polarisation remains aligned to the birefringent axis (dashed lines) and flips at points for which the gain is surpassed by that of the other birefringence axis. The offset from the fast and slow axes caused by the presence of small amount of optical rotation is also

correctly predicted. The small discrepancies between the modelled and measured polarisations ($< 3^\circ$) are attributed to errors in measuring the value of circular birefringence and fast axis orientation.

Since all polarisation measurements reported to date have corresponded to the extreme cases producing linearly polarised output, our work predicts conditions that are expected to yield elliptical output. It is noted that the region of high ellipticity places tight constraints on the exact values of R and ξ as shown in Fig. 6.

5. Conclusion

We have used a Jones formalism to calculate polarisation modes in lasers containing non-collinear anisotropic gain and birefringent axes, a scenario that occurs in diamond Raman lasers. The model describes 3 main regimes: A gain dominated regime in which linear output polarisations are observed along the high gain axis. A birefringence dominant regime in which linear polarisations are produced in directions along the fast and slow axis depending upon which is more closely aligned to the high gain axis. And a transition region producing elliptical outputs when the effects of gain and birefringence are in near balance. The model also considers the role of optical rotation in the gain medium, which is found to occur in some diamond samples. In standing wave resonators the rotation causes an angular offset in the polarisation behaviour; however, for unidirectional ring lasers, even small amounts of optical rotation lead to elliptical output.

The theory also applies to other anisotropic systems such as silicon Raman lasers (which share crystal class with diamond) and potentially inversion lasers that have a combination of strongly anisotropic gain and birefringence. Extension to other systems is straightforward provided the gain has an orthogonal basis where the polarisation components amplify independently.

Funding

Australian Research Council (ARC) (DP150102054, LP160101039); U.S. Air Force Research Laboratory (FA2386-18-1-4117).

Acknowledgments

The authors would like to acknowledge helpful comments from A. Sabella and H. Jasbeer.

References

1. W. Koechner and D. Rice, "Effect of birefringence on the performance of linearly polarized YAG:Nd lasers," *IEEE J. Quantum Electron.* **6**, 557–566 (1970).
2. S. D. Jackson and J. A. Piper, "Thermally induced strain and birefringence calculations for a Nd:YAG rod encapsulated in a solid pump light collector," *Appl. Opt.* **35**, 1409–1423 (1996).
3. H. Jasbeer, R. J. Williams, O. Kitzler, A. McKay, S. Sarang, J. Lin, and R. P. Mildren, "Birefringence and piezo-Raman analysis of single crystal CVD diamond and effects on Raman laser performance," *J. Opt. Soc. Am. B* **33**, B56–B64 (2016).
4. H. Kogelnik and T. Li, "Laser beams and resonators," *Appl. Opt.* **5**, 1550–1567 (1966).
5. V. Y. Molchanov and G. V. Skrotskii, "Matrix method for the calculation of the polarization eigenstates of anisotropic optical resonators," *Sov. J. Quantum Electron.* **1**, 3–26 (1972).
6. A. J. Kemp, G. J. Friel, T. K. Lake, R. S. Conroy, and B. D. Sinclair, "Polarization effects, birefringent filtering, and single-frequency operation in lasers containing a birefringent gain crystal," *IEEE J. Quantum Electron.* **36**, 228–235 (2000).
7. S. Helmfrid and K. Tatsuno, "Stable single-mode operation of intracavity-doubled diode-pumped Nd:YVO₄ lasers: theoretical study," *J. Opt. Soc. Am. B* **11**, 436–445 (1994).
8. S. Zhang, Y. Tan, and S. Zhang, "Effect of gain and loss anisotropy on polarization dynamics in Nd:YAG microchip lasers," *J. Opt.* **17**, 045703 (2015).
9. J. Martin-Regalado, F. Prati, M. S. Miguel, and N. B. Abraham, "Polarization properties of vertical-cavity surface-emitting lasers," *IEEE J. Quantum Electron.* **33**, 765–783 (1997).
10. M. San Miguel, Q. Feng, and J. V. Moloney, "Light-polarization dynamics in surface-emitting semiconductor lasers," *Phys. Rev. A* **52**, 1728–1739 (1995).

11. A. Gahl, S. Balle, and M. S. Miguel, "Polarization dynamics of optically pumped vesels," *IEEE J. Quantum Electron.* **35**, 342–351 (1999).
12. M. Alouini, J. Frougier, A. Joly, G. Baili, D. Dolfi, and J.-M. George, "VSPIN: a new model relying on the vectorial description of the laser field for predicting the polarization dynamics of spin-injected V(e)CSELs," *Opt. Express* **26**, 6739–6757 (2018).
13. R. Loudon, "The Raman effect in crystals," *Adv. Phys.* **13**, 423–482 (1964).
14. T. Basiev, A. Sobol, P. Zverev, L. Ivleva, V. Osiko, and R. Powell, "Raman spectroscopy of crystals for stimulated Raman scattering," *Opt. Mater.* **11**, 307–314 (1999).
15. E. Hecht, *Optics* (Addison-Wesley Longman, Inc., 2002).
16. A. Sabella, J. A. Piper, and R. P. Mildren, "1240 nm diamond Raman laser operating near the quantum limit," *Opt. Lett.* **35**, 3874–3876 (2010).
17. Y. R. Shen and N. Bloembergen, "Theory of stimulated Brillouin and Raman scattering," *Phys. Rev.* **137**, 1787–1805 (1965).
18. O. Kitzler, A. McKay, and R. P. Mildren, "Continuous-wave wavelength conversion for high-power applications using an external cavity diamond Raman laser," *Opt. Lett.* **37**, 2790–2792 (2012).
19. R. J. Williams, J. Nold, M. Strecker, O. Kitzler, A. McKay, T. Schreiber, and R. P. Mildren, "Efficient Raman frequency conversion of high-power fiber lasers in diamond," *Laser & Photonics Rev.* **9**, 405–411 (2015).
20. H. Hurwitz and C. R. Jones, "A new calculus for the treatment of optical systems II. Proof of three general equivalence theorems," *J. Opt. Soc. Am.* **31**, 493–499 (1941).
21. C. R. Jones, "New calculus for the treatment of optical systems. VII. Properties of the N-matrices," *J. Opt. Soc. Am.* **38**, 671–685 (1948).